Atomic structure study of the pyrochlore Yb$_2$Ti$_2$O$_7$ and its relationship with low-temperature magnetic order

Ali Mostaed,[1,*] Geetha Balakrishnan,[1] Martin Richard Lees,[1] Yukio Yasui,[2] Lieh-Jeng Chang,[3] and Richard Beanland[1]

[1]*Department of Physics, University of Warwick, Gibbet Hill Road, CV4 7AL, Coventry, United Kingdom*
[2]*Department of Physics, Meiji University, Kawasaki 214-8571, Japan*
[3]*Department of Physics, National Cheng Kung University, Tainan 70101, Taiwan*

There has been great interest in the magnetic behavior of pyrochlore oxides with the general formula $A_2B_2O_7$, in which rare-earth (A) and transition metal (B) cations are ordered on separate interpenetrating lattices of corner-sharing tetrahedra. Such materials exhibit behaviors including quantum spin-ice, (quantum) spin-liquid, and ordered magnetic ground states. Yb$_2$Ti$_2$O$_7$ lies on the boundary between a number of competing magnetic ground states. Features in the low-temperature specific heat capacity that vary in sharpness and temperature from sample to sample suggest that, in some cases, the magnetic moments order, while in others, the moments remain dynamic down to temperatures as low as ∼16 mK. In this paper, three different Yb$_2$Ti$_2$O$_7$ samples, all grown by the optical floating zone technique but exhibiting quite different heat capacity behavior, are studied by aberration-corrected scanning transmission microscopy (STEM). Atomic-scale energy-dispersive x-ray analysis shows that a crystal with no specific heat anomaly has substitution of Yb atoms on Ti sites (stuffing). We show that the detailed intensity distribution around the visible atomic columns in annular dark field STEM images is sensitive to the presence of nearby atoms of low atomic number (in this case oxygen) and find significant differences between the samples that correlate both with their magnetic behavior and measurements of Ti oxidation state using electron energy loss spectroscopy. These measurements support the view that the magnetic ground state of Yb$_2$Ti$_2$O$_7$ is extremely sensitive to disorder.

I. INTRODUCTION

Pyrochlore oxides with the general formula $A_2B_2O_7$, in which A is a rare-earth ion and B is a transition metal, exhibit a variety of interesting magnetic properties [1]. The A and B cations lie on distinct but interpenetrating lattices of corner-sharing tetrahedra. Such a lattice is incompatible with a simple organization of magnetic moments and leads to geometric frustration [1]. By analogy with the large ground-state entropy of crystalline H$_2$O [2], which has an oxygen lattice of corner-sharing tetrahedra, the ground states of many magnetic $A_2B_2O_7$ materials have been proposed to be a spin-ice [1]. In a spin-ice, each tetrahedron has two spins pointing inwards and two outwards (so-called ice rules [1,3]). Other unusual behaviors have also been observed in $A_2B_2O_7$ pyrochlores, including spin-glass [4–6], and spin-liquid [4] states, as well as magnetic configurations modified by quantum fluctuations [1,7–10]. The qualities of any given $A_2B_2O_7$ compound are principally dictated by the elements A and B, but can be strongly altered by structural defects, particularly stuffing of magnetic A^{3+} ions onto nonmagnetic B^{4+} sites and oxygen, A or B site vacancies [1,7–10].

Here, we examine Yb$_2$Ti$_2$O$_7$. The picture for this material is complicated by reports of different results for polycrystalline and single crystal samples and for different samples with nominally identical form, stoichiometry, and structure [11–13]. An early paper found a peak in the temperature dependence of the heat capacity of Yb$_2$Ti$_2$O$_7$ at 214 mK [14], consistent with later neutron scattering, muon spectroscopy, and magnetization studies that associate the heat capacity anomaly with a

first-order transition to ferromagnetic long-range magnetic order [13,15–18] with a collinear or nearly collinear magnetic structure [15,16], an icelike splayed ferromagnetic structure [19] or all-in/all-out splayed ferromagnetic structure [20]. Other papers have proposed that this system is a quantum spin-ice [11,12,21,22] or quantum spin-liquid [23,24] or adopts a ground state with short-range correlations where the magnetic moments continue to fluctuate down to temperatures as low as 16 mK [25–27].

The origin of these discrepancies probably lies in subtle structural differences and a proximity to one or more magnetic phase boundaries [28–30]. In such a case, even small perturbations in exchange parameters, which could be driven by a number of (competing) factors, might be expected to produce significant changes in the nature of the magnetic ground state. Small differences in stoichiometry are known to have significant effects on the properties of Yb$_2$Ti$_2$O$_7$. For many rare-earth titanate pyrochlores, stuffing of excess A^{3+} ions onto the Ti^{4+} site happens much more readily than antistuffing of Ti onto the A site [31]. This also seems to be the case for Yb$_2$Ti$_2$O$_7$; Ross *et al.* found that neutron diffraction of Yb$_2$Ti$_2$O$_7$ prepared as a powder was best fit by a stoichiometric model, while a float-zone grown single crystal (prepared from stoichiometric starting materials) was best described by stuffing of Yb onto 2.3% of Ti sites, rather than Ti vacancies or antistuffing [11]. However, Baroudi *et al.* in a synchrotron x-ray diffraction paper proposed that Yb, being the smallest of the rare-earth atoms, could swap with Ti, producing up to 2% antisite defects in their Yb$_2$Ti$_2$O$_7$ powders [31].

We employ aberration-corrected scanning transmission electron microscopy (STEM) to investigate three differ-
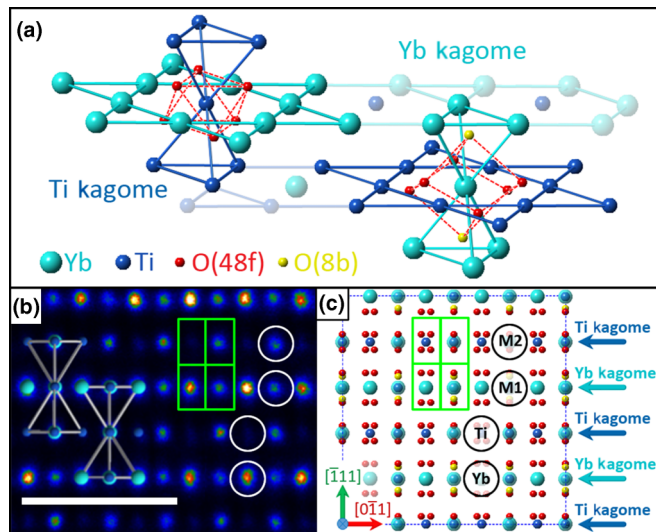
*a.mostaed@warwick.ac.uk

FIG. 1. (a) The pyrochlore structure of $Yb_2Ti_2O_7$ (see text for details). (b) [2 1 1] ADF-STEM image of $Yb_2Ti_2O_7$ with Yb and Ti tetrahedra overlaid (scale bar is 1 nm). Four different types of atom columns are visible, marked by circles. The Yb columns are the brightest, followed by mixed columns $M1$ and $M2$, while the Ti columns are the faintest. (c) Corresponding projection of the crystal structure showing the Kagome layers and the four different types of atom column. Voronoi cells, used for measurement of intensities in the image, are illustrated in green in (b) and (c).

ent samples that have quite different low-temperature heat capacity behavior, in conjunction with atomically resolved energy-dispersive x-ray spectroscopy (EDX) and electron energy loss spectroscopy (EELS). While diffraction studies, such as those mentioned above, measure average structure, electron microscopy at atomic resolution offers the opportunity to directly observe defects such as stuffing and atom swapping between cation sites as well as providing average measurements from regions several nanometers in size. We find significant differences between the samples that correlate with their magnetic behavior.

In order to interpret atomic resolution images of $Yb_2Ti_2O_7$, the pyrochlore structure ($Fd\bar{3}m$) [32] must be considered. One way to understand the structure of $Yb_2Ti_2O_7$ is examination of {1 1 1} planes as shown in Fig. 1(a). On these planes, sheets of metal atoms have a hexagonal Kagome pattern and alternate between Yb^{3+} (light blue) and Ti^{4+} (dark blue) in Fig. 1. In each Yb layer, Ti atoms sit at the center of an Yb hexagon [top, Fig. 1(a); most oxygen atoms have been omitted for clarity]. These Ti atoms also lie at the vertex of a pair of opposing Ti tetrahedra that link to the Ti Kagome layers above and below. A similar pattern is found for Yb atoms in the Ti Kagome layer [bottom, Fig. 1(a)]. Each metal atom is surrounded by an octahedron of oxygen ions that either lie on a Wyckoff f site (red) or b site (yellow). Note that all the cations of the same type are symmetrically identical, and this pattern is found on all of the symmetrically equivalent {1 1 1} layers. Crystallographic parameters for a perfect $Yb_2Ti_2O_7$ crystal [33] are listed in Table SI in the Supplemental Material [34].

When viewed along [2 1 1], one set of {1 1 1} planes is seen edge on. In this projection, there are four types of heavy

atom columns [Fig. 1(c)], those containing only Yb, those containing only Ti, and two different mixed (M) columns containing 50% Ti and 50% Yb. The difference in M columns arises because there are twice as many oxygen atoms, around 50:50 columns in the Yb Kagome layer ($M1$) in comparison with 50:50 columns in the Ti Kagome layer ($M2$). In this projection, the oxygen atom columns lie ~72 pm from the $M1$ columns, while those next to $M2$ columns lie at a distance of ~49 pm. The large difference in scattering power between oxygen and the metal atom columns with high Z in such images effectively renders oxygen invisible in comparison with adjacent atoms [35–37].

Our interest lies in the purity of the Yb and Ti sublattices—and the effect on adjacent oxygen atoms—that may result from the presence of an Yb atom on a Ti site, or vice versa. We thus consider a simple model in which an atomic column, which is nominally comprised completely of atoms of type X in perfect material, has some atoms replaced by others of type Y. Now, moving atoms between different cation sublattices must involve changes in oxidation state and/or anion populations in order to maintain charge balance; rearrangements of oxygen atoms or oxygen vacancies may be necessary. We will return to these points later, but begin by assuming that there is no correlation between the different substitution sites, i.e. that there is no clustering or repulsion between substituted sites and there are no vacancies, interstitials, or impurity atoms. In such a simple case, with a probability p_{XY} for an atom of type X to be replaced by one of type Y, the probability of finding a column of n atoms which contains m type Y atoms is given by the binomial distribution, i.e.

$$P\binom{n}{m} = \frac{n!}{m!(n-m)!}(1-p_{XY})^{n-m}p_{XY}^m. \quad (1)$$

Thus, even stuffing of a few percent [11,31] should be detectable in compositional analysis sensitive to single atoms at the atomic scale (Fig. 2). For the [2 1 1] zone axis and a moderate specimen thickness of 45 nm, replacement of 1% gives more than 50% of atomic columns that contain at least
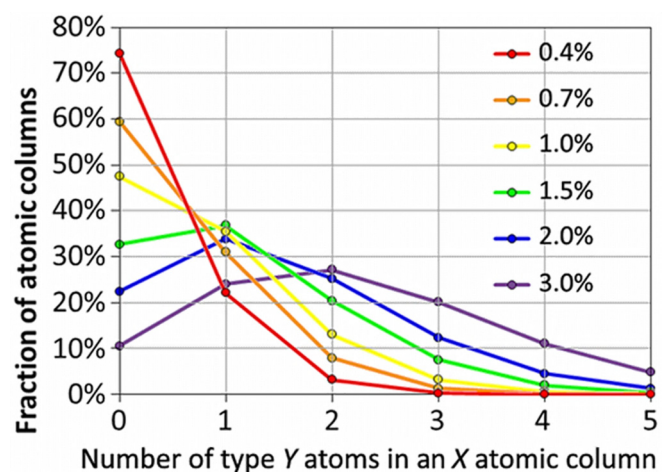

FIG. 2. The fraction of columns with 73 atoms that have between zero and five foreign atoms predicted by [Eq. (1)], for different amounts of average atom swapping (0.4 to 3%). This is equivalent to a [2 1 1] $Yb_2Ti_2O_7$ specimen with thickness 45 nm.

one foreign atom (yellow curve). Even if only 0.4% of atoms are replaced by a different type, more than 20% of atomic columns will have one foreign atom (red curve). Conversely, unaffected columns only form a small fraction of the image if significant amounts of stuffing occur; only 10% have no foreign atom at a stuffing of 3% (violet curve). Importantly, at stuffing fractions of a few percent, adjacent columns with widely differing substitutions should be quite common.

Aberration-corrected STEM images such as Fig. 1(b) contain quantifiable composition information [38,39] due to the atomic number sensitivity of high-angle (Rutherford) electron scattering [40–43]. Thus, it may be expected that analysis of image intensities may provide data that is sensitive to the composition of the Yb and Ti sublattices. Several schemes for quantitative analysis of annular dark field (ADF) images have been proposed. LeBeau *et al.* [44] have used the maximum pixel intensity in the vicinity of the centroid of each atom image, while Van Aert *et al.* [45] assume the intensity of each atom column is a cylindrically symmetric two-dimensional (2D) Gaussian and perform a least-squares fit. Neither of these is appropriate for the current case, where unresolved oxygen atoms lie close to the metal atoms; rather, we use intensities integrated over a Voronoi cell surrounding the atom column of interest. A Voronoi cell is an area bounded by the perpendicular bisectors of all vectors that link adjacent atom columns [40,46–48]. The mean integrated intensity in a Voronoi cell is proportional to the scattering cross-section of the atom column, while retaining a useful degree of insensitivity to exact experimental conditions such as defocus and spatial incoherence [43]. For the [2 1 1] projection, the Voronoi cell is a simple rectangle as shown in Figs. 1(b) and 1(c). Nevertheless, the contrast of atomic columns may not be directly interpretable in terms of composition, e.g. due to static atomic displacements [49,50] that may be a result of stuffing.

Here, we show that O vacancies, along with stuffing of Yb atoms onto the Ti sites, are responsible for the breakdown of the long-range magnetic ordering in $Yb_2Ti_2O_7$ pyrochlore, resulting in a material that exhibits only short-range order or in which magnetic ordering is absent down to the lowest temperatures measured.

II. METHODS

We investigated three $Yb_2Ti_2O_7$ single crystals prepared by the floating zone method with quite different low-temperature specific heat characteristics. Stoichiometric quantities of Yb_2O_3 and TiO_2 powder were mixed, pressed into rods, and then sintered at 1150 °C (Sample 1 and Sample 3) or 1350 °C (Sample 2) for 24 h. Using these rods, single crystals were grown in air at a rate of 1.5 mm/h (Sample 1 and Sample 3) or 2 mm/h (Sample 2). The crystals had a typical diameter of ∼6 mm and a length of 20 to 30 mm. The samples were used in previous papers [15,16,18]. As shown in Fig. 3, Sample 1 exhibits a sharp transition at ∼200 mK, consistent with the onset of long-range magnetic order, typical of stoichiometric powder samples although at a reduced temperature. The long-range ferromagnetic order in Sample 1 is confirmed by both single crystal neutron diffraction [15,16] and ac and dc magnetometry, where a clear signature of a transition to an ordered state is observed [18]. Sample 2 shows two relatively
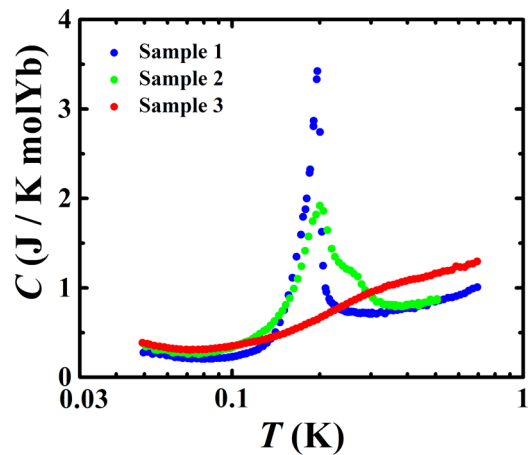

FIG. 3. Specific heat as a function of temperature for the three $Yb_2Ti_2O_7$ samples in zero magnetic field [15,16,18].

broad anomalies at ∼200 and 280 mK. This type of behavior could be explained by short-range magnetic ordering, with the magnetic correlation length limited by defects [11]. Finally, Sample 3 exhibits no clear specific heat anomaly, consistent with a disordered magnetic state, and is thus expected to have significant stuffing of Yb^{3+} onto the Ti^{4+} sites [11]. Samples 2 and 3 have both been examined using neutron diffraction. Neither sample exhibited any clear additional intensity on structural Bragg peaks indicative of ferromagnetic long-range order.

In order to avoid any issues associated with sample inhomogeneity and to be able to compare the microscopy and heat capacity results directly, the TEM specimens were taken from the same thin sections of the crystal used for the heat capacity measurements. The TEM specimens were prepared using standard routes, i.e. mechanical grinding and polishing followed by ion milling to electron transparency using Ar^+ at 6 keV. Surface damage was minimized by a final low-energy milling step at 500 eV. Images were obtained with a doubly corrected JEOL ARM200F microscope at 200 kV. Defect-free, flat, and uniform regions of interest were selected with thicknesses characterized using low-loss EELS [51], chosen to be $t/\lambda \approx 0.61$, i.e. ∼45 nm. In order to obtain data with a good signal-to-noise ratio, unaffected by specimen drift, up to 60 images were collected sequentially, all with a short time of 10 μs/pixel. The resulting set of images was aligned using normalized cross-correlation and summed to produce high-quality, low-noise data.

At small scattering angles, i.e. when the inner angle of the ADF detector is only a little larger than the probe convergence angle α, coherent diffraction effects can produce strain contrast that is very sensitive to crystal orientation that compromises the ability to relate intensities to atomic number [38]. Here, therefore, for images intended to be sensitive to composition, we use an ADF detector inner angle at least 4.6 times the probe convergence angle α, giving a scattered intensity proportional to a small power of the atomic number, $Z^{1.5}$ to Z^2 [52,53]. For images that show greater sensitivity to the configurations of oxygen atoms, we use an ADF detector inner angle of only ∼2.4α. Data were normalized to the incident beam intensity using calibrated brightness/contrast levels, a map of the ADF
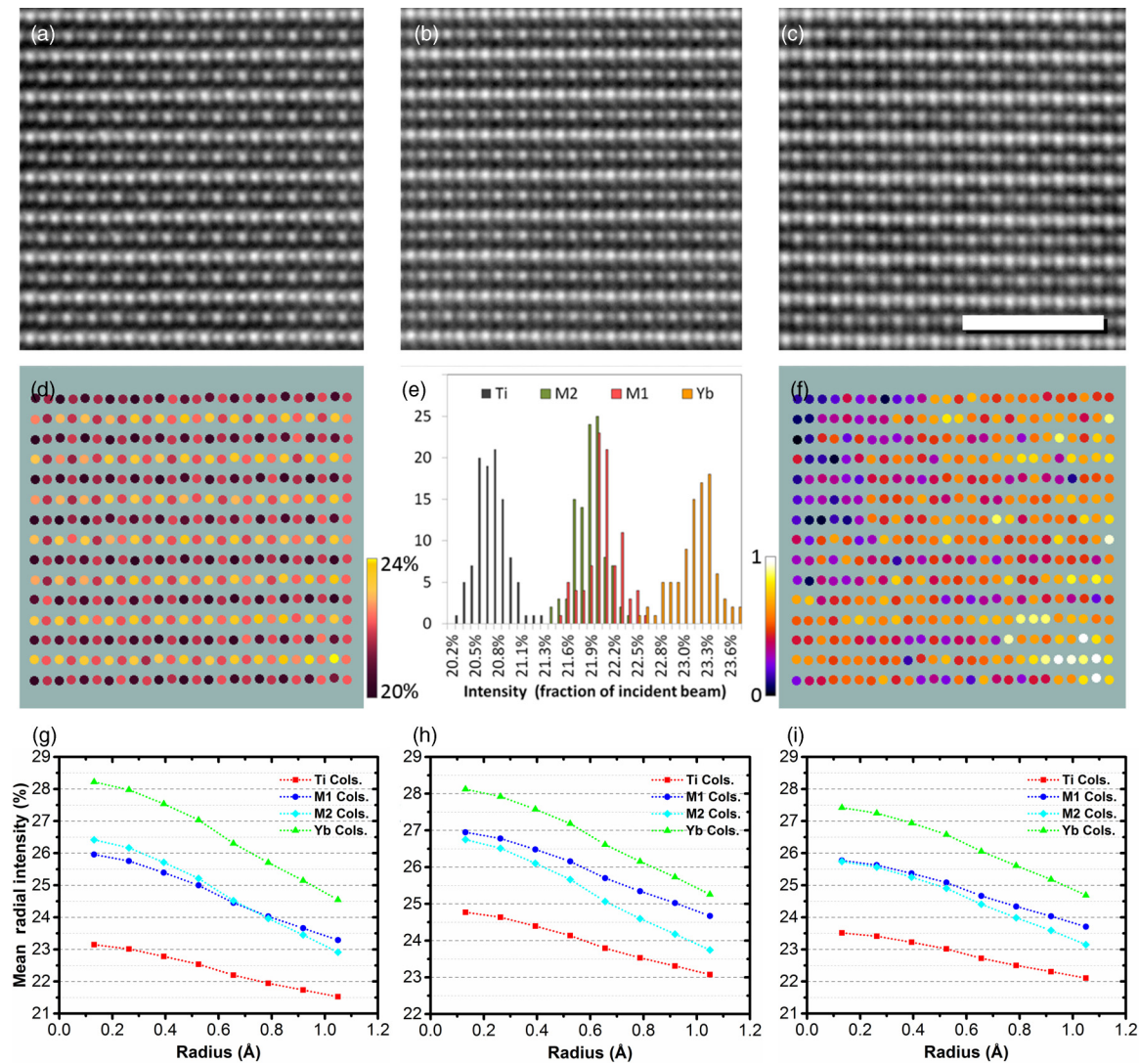
FIG. 4. ADF-STEM images taken with an ADF detector inner angle of 2.4α, (a) Sample 1, (b) Sample 2, and (c) Sample 3, viewed along [2 1 1] (scale bar is 2 nm). (d) Extracted mean integrated intensities from (a) using Voronoi cells centered on each atomic column, plotted as a histogram in (e). Normalizing the intensities from each sublattice separately shows the intensity variations across the image (f). Mean radial intensity profiles for (g) Sample 1, (h) Sample 2, and (i) Sample 3.

detector response and an image of the diffraction pattern falling on the detector, following an approach similar to that of LeBeau *et al.* [54]. Energy-dispersive x-ray spectroscopy measurements were obtained with a windowless Oxford Instruments X-max 100 silicon drift x-ray detector. Electron energy loss spectra were obtained with a Gatan Quantum EELS system operating in dual EELS mode, allowing correction of zero-loss offsets and removal of multiple scattering from high-energy core-loss edges by Fourier-log deconvolution calculated from the low-loss spectrum. Image simulations were performed with QSTEM [55] and STEMsim [56] multislice to compare with experimental data.

III. RESULTS

A. ADF-STEM intensities

Representative [2 1 1] ADF-STEM images from the three samples are shown in Figs. 4(a)–4(c), taken with an ADF detector inner angle of 2.4α. Voronoi intensity measurements

for Sample 1 are shown in Figs. 4(d)–4(f) (equivalents for Samples 2 and 3 are shown in Fig. S1 provided in the Supplemental Material [34]). The four sublattices are readily distinguished in the false color image Fig. 4(d) and the intensity histogram Fig. 4(e). The higher mean intensity of $M1$ in comparison with $M2$ is caused by the presence of four oxygen columns in the Voronoi cell of every $M1$ column in comparison with two for $M2$ [Fig. 1(c)]. Thus, even though oxygen atoms cannot be resolved in these ADF-STEM images, it is clear that their effect can be seen in quantitative intensity measurements.

One might hope that the range of intensities in the histograms for each type of atom would be governed in some way by Eq. (1). However, if the four sublattice intensities are each normalized separately to a range between zero and one [Fig. 4(f)], it becomes apparent that there is a systematic variation across the image, presumably due to a small variation in specimen thickness. The width of the intensity histograms in Fig. 4(e) is thus mainly caused by this thickness variation rather than atomic substitutions. Similar
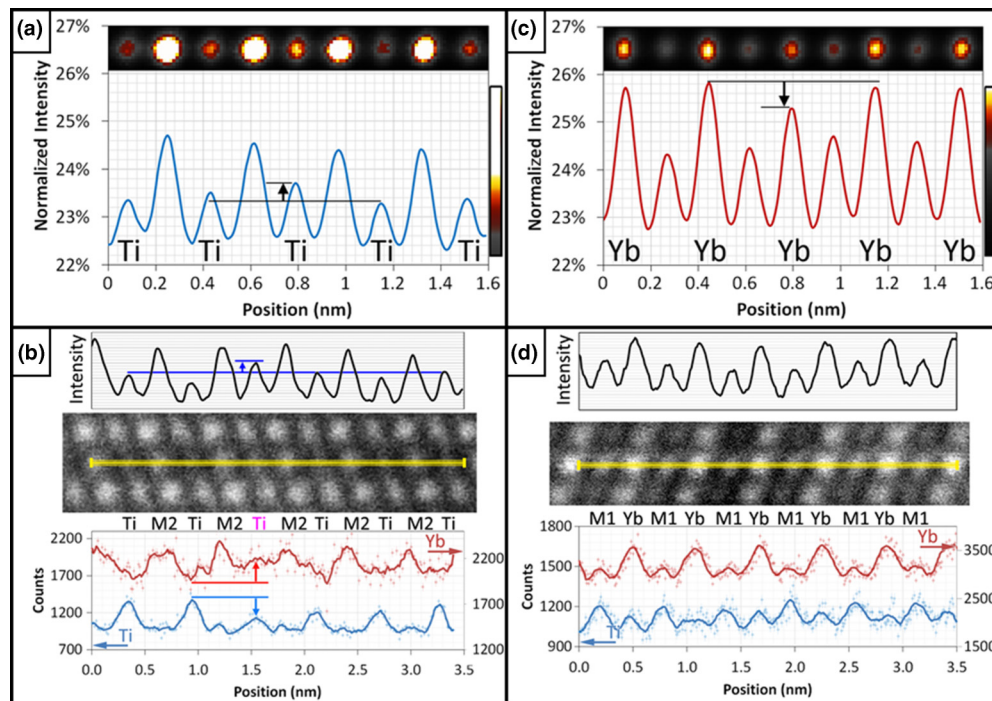
FIG. 5. ADF-STEM and EDX analysis of Sample 3. (a) Anomalously bright intensity from a Ti column. (b) Atomic scale EDX analysis along a line of Ti and $M2$ atom columns, showing a decrease in Ti signal and increase in Yb signal at an anomalously bright Ti atom column. (c) Anomalously weak intensity from an Yb atom column. (d) Atomic scale EDX analysis along a line of Yb and $M1$ atom columns.

variations are present for Samples 2 and 3 (see Supplemental Material Fig. S1) [34]. These thickness variations and/or damage/contamination of the specimen surface are sufficient to mask statistical measurements of stuffing, or antistuffing, from the ADF intensities of atomic columns, i.e. changes in the number of atoms per column n easily produce differences that are equal to or larger than the effect of a few atomic substitutions.

The difference in $M1$ and $M2$ column intensities indicates a sensitivity of ADF data to nearby oxygen atoms. We therefore investigated mean radial intensity as a function of distance from the center of the visible atom columns, averaged over all equivalent columns in the images of Figs. 4(a)–4(c). These mean radial intensity profiles are shown in Figs. 4(g)–4(i), where the center of the atom column is at the origin and the mean radial intensity decays following a quasi-Gaussian profile. In Sample 1, the $M2$ columns have a higher peak intensity [Fig. 4(g)], consistent with oxygen atom columns close to their centers (49 pm in the nominal structure). The radial intensity of the $M1$ columns decays more slowly, consistent with more oxygen atom columns at larger distances (72 pm in the nominal structure). The intensity of $M1$ columns exceeds that of $M2$ columns at a radius of $\sim$65 pm (see also Fig. S2(a) and Fig. S3 in the Supplemental Material [34]). The same trend is observed in multislice simulations of the nominal $Yb_2Ti_2O_7$ structure (Fig. S2(d) in the Supplemental Material [34]), with the intensity at $M2$ columns becoming smaller than that of $M1$ columns at a certain radius depending the sample thickness.

Interestingly, the higher peak intensity of $M2$ columns shown in Fig. 4(g) is only found in Sample 1; for samples 2 and 3, as illustrated in Figs. 4(h) and 4(i), the radial intensity of $M2$

never exceeds that of $M1$ (see also Fig. S2 in the Supplemental Material [34]). This effect could be caused by fewer oxygen atoms in the Wyckoff f site or their movement away from $M2$ columns, which would reduce the $M2$ intensity at small radii, and/or movements of f- and b-site oxygen atoms closer to $M1$ columns, which would increase their intensity at small radii.

B. Atomic resolution EDX

Sample 3 is the most likely of the three samples to exhibit stuffing. Atomic columns with anomalous contrast in comparison with their neighbors in ADF images were observed, as shown in Fig. 5. Anomalously bright Ti columns, consistent with stuffing of Yb onto Ti sites were observed [Fig. 5(a)] as well as anomalously dark Yb columns, consistent with antistuffing of Ti onto Yb sites [Fig. 5(c)]. These were examined with atomic resolution EDX. Figure 5(b) shows an EDX line scan across an anomalously bright Ti column, made using Ti $K\alpha$ (4.51 keV) and Yb $L\alpha$ (7.41 keV) x-rays. There is an obvious drop in Ti signal and an increase in the Yb signal for the brighter column in comparison with the others, particularly those to the left. The correlation between bright atom column contrast and a lower Ti/higher Yb signal was observed several times (see Fig. S4 in the Supplemental Material [34]) and is direct evidence for stuffing in this sample. Figure 5(d) shows a line of Yb-$M1$ columns, in which a small Ti signal can be seen at each Yb column as well as the expected signal at the $M1$ columns. While this may indicate antistuffing of Ti onto Yb sites, it is also possible that a small amount of specimen drift (0.2 nm) during acquisition introduced some signal from the adjacent Ti-$M2$ row of atoms.
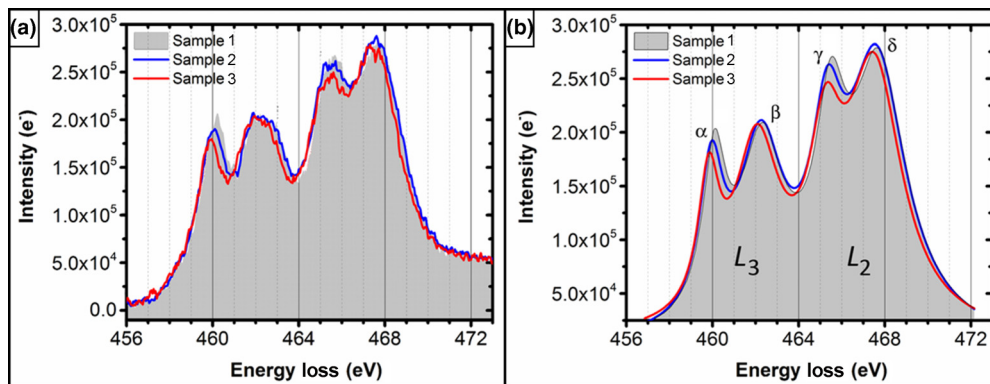
FIG. 6. (a) Experimental EEL Ti $L_{3,2}$ spectra of the three samples ($t/\lambda = 0.30$). (b) Lorentzian curves fitted to the experimental EEL spectra shown in (a).

C. EELS

Analysis of $Yb_2Ti_2O_7$ at atomic resolution using EELS is possible using the Ti-$L_{3,2}$ edge at ~ 450 eV and the Yb-$N_{4,5}$ edge at 185 eV, although spatial resolution is limited for the latter due to delocalization effects [51], limiting the analysis to the [1 1 0] zone axis. Nevertheless, electron energy loss near-edge structure (ELNES) spectra can be used to obtain information on Ti bonding configurations [57–59]. Metallic Ti shows two white lines L_3 and L_2 at 456 and 462 eV, due to electron transitions from $2p_{3/2}$ and $2p_{1/2}$ subshells to unoccupied $3d$ states, respectively. In titanium oxides, the number of peaks in the Ti-$L_{3,2}$ ELNES spectrum depends on valence state, coordination, and site symmetry of the Ti atoms [58]. In materials with a Ti oxidation state of $+4$, like $Yb_2Ti_2O_7$, titanium core-holes created by excitation of $2p$ core electrons can be poorly screened since there is no electron in the Ti^{4+} conduction band. Consequently, both L_3 and L_2 edges are shifted to higher energy losses than for metallic Ti [58]. Octahedral coordination of Ti atoms with oxygen splits the degenerate unoccupied $3d$ states into a lower energy $2t_{2g}$ molecular energy level and a higher $3e_g$ level [60]. Hence, in $Yb_2Ti_2O_7$, the Ti L_3 and L_2 edges both consist of two white lines, α and β for L_3 and γ and δ for L_2. In fact, for each edge, the first (α, γ) and second (β, δ) peaks are due to transitions from the $2p$ state to the $2t_{2g}(\pi^*)$ and $3e_g(\sigma^*)$ oxide levels, respectively.

A decrease in Ti valence, for example, due to oxygen vacancies, has two effects on Ti-$L_{3,2}$ ELNES: (a) a systematic shift to lower energies of ~ 2 eV per valence state [58] and (b) the intensity ratios I_β/I_α, I_δ/I_γ, and I_β/I_δ all trend to larger values [57,58]. These changes are very sensitive indicators of change in Ti valence.

The experimental spectra from the three samples are shown in Fig. 6(a). Peak energies, extracted by fitting the data to four Lorentzian curves [Fig. 6(b)], as well as intensity ratios are listed in Table I. All of these indicators show that the Ti valence drops from Sample 1 to Sample 2 and still further for Sample 3.

IV. DISCUSSION

The above results are in agreement with the previous studies of $Yb_2Ti_2O_7$ that found evidence for Yb stuffing onto

Ti sites, even in nominally stoichiometric material, and that more stuffing correlates with more diffuse peaks in specific heat capacity. Ross *et al.* [11] discounted oxygen vacancies as the structural origin of the varying magnetic behavior of $Yb_2Ti_2O_7$, based on the lack of change in materials subjected to long anneals in an oxygen-rich environment. However, here, we find changes in Ti valence that indicate an increasing oxygen vacancy content as stuffing and/or cation site swapping increases from Sample 1 to Sample 3, and this correlates with the changes in magnetic behavior. These apparently contradictory findings can be reconciled by noting that, on average, replacing two Ti^{4+} atoms by Yb^{3+} will be balanced by one O^{2-} vacancy if the Yb sublattice remains unchanged. Stuffing therefore may change the equilibrium oxygen stoichiometry in $Yb_2Ti_2O_7$, which is quite different to a nonequilibrium oxygen deficiency that can be remedied by annealing.

The EELS data (Fig. 6) thus show a correlation between magnetic properties and oxidation state. In order to link this to the differences in intensity profiles we observe in ADF-STEM data (Fig. 4) and the effects of stuffing, it is necessary to consider the position of the oxygen atoms in the crystal structure. One way to do this is to divide the crystal into regular tetrahedral and octahedral volumes (Fig. 7). Each cation sits at the vertex of six edge-sharing tetrahedra and six corner-sharing octahedra. These are shown for an Yb atom in Figs. 7(a) and 7(b); the octahedra are empty, while each tetrahedron contains an oxygen atom. There are two types of tetrahedron around an Yb atom, shown in colored shading in Fig. 7(b); two tetrahedra are comprised of four Yb^{3+} ions *4Yb*, with a Wyckoff

TABLE I. Ti ELNES energies and intensity ratios for the three $Yb_2Ti_2O_7$ samples.

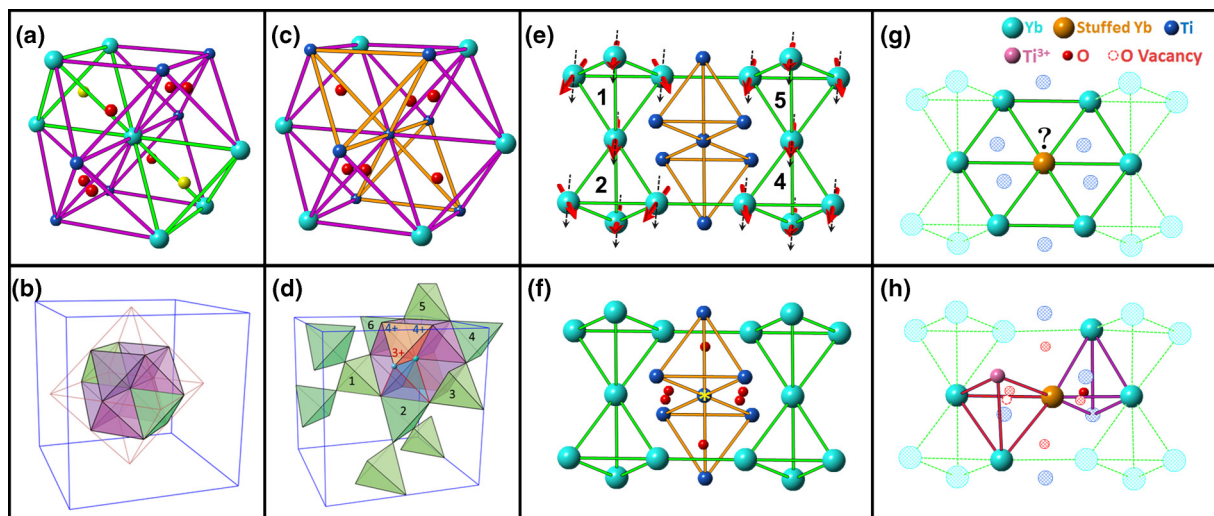|		Sample 1	Sample 2	Sample 3
	E_α	460.08 ± 0.01	459.94 ± 0.01	459.82 ± 0.01
L_3	E_β	462.32 ± 0.02	462.23 ± 0.02	462.06 ± 0.02
	I_β/I_α	2.13 ± 0.13	2.33 ± 0.13	2.91 ± 0.17
	E_γ	465.48 ± 0.02	465.32 ± 0.02	465.24 ± 0.02
L_2	E_δ	467.74 ± 0.02	467.63 ± 0.02	467.52 ± 0.02
	I_δ/I_γ	2.64 ± 0.15	3.13 ± 0.19	2.96 ± 0.18

FIG. 7. Cation tetrahedra in $Yb_2Ti_2O_7$. (a) Ball and stick model showing the eight cation tetrahedra that have a common vertex at an Yb atom. (b) The same tetrahedra, color-coded as *2Ti2Yb* (purple) and *4Yb* (green). (c) Ball and stick model showing the eight cation tetrahedra that have a common vertex at a Ti atom. (d) The effect of stuffing an Yb^{3+} atom onto the Ti^{4+} site. The six *2Ti2Yb* tetrahedra (purple) become *1Ti3Yb*, and the two *4Ti* (orange) become *3Ti1Yb*. Stuffing produces an oxygen vacancy in one of the surrounding *1Ti3Yb* tetrahedra (highlighted in red) and the conversion of an adjacent Ti atom from 4^+ to 3^+. The network of magnetic *4Yb* tetrahedra are also shown, with six numbered *4Yb* tetrahedra surrounding the stuffed atom site. (e) The Yb tetrahedra shown in (d) without any stuffing and possible all-in/all-out [20] (the left Yb tetrahedra) and two-in/two-out [20] (the right Yb tetrahedra) splayed ferromagnetic configurations (black arrows are along [1 0 0]). (f) Position of the oxygen atoms in the vicinity of the Ti atom (marked by a yellow star) before stuffing. (g) Frustrated triangular lattice of magnetic cations formed by replacing a Ti atom with Yb. (h) Formation an oxygen vacancy and reduction of a Ti^{4+} cation to Ti^{3+} as a consequence of stuffing.

b-site O^{2-} atom at their centers (green), while the remaining six (purple) have two Yb and two Ti atoms *2Ti2Yb* and a Wyckoff *f*-site O^{2-} atom, displaced well off-center, close to the midpoint of the edge connecting the Ti atoms. A similar structure surrounds the Ti atoms, except in this case there are six *2Ti2Yb* tetrahedra and two *4Ti* tetrahedra, comprised of four Ti^{4+} ions with no oxygen atom inside.

Stuffing will change all eight tetrahedra that surround the affected site. A possible structure that results from replacing a Ti^{4+} atom with Yb^{3+} is shown in Fig. 7(d). The six *2Ti2Yb* tetrahedra become *1Ti3Yb* tetrahedra (purple) and the two *4Ti* tetrahedra change to *3Ti1Yb*. No other ytterbium titanates have been documented that could be used as a guide to the structural changes that will result, but we note that Ti-O bond lengths are much shorter than Yb-O bond lengths (∼1.95 vs ∼2.3 Å) and Ti-O-Ti bond angles tend to be approximately 130°. Thus, oxygen atoms in the *1Ti3Yb* tetrahedra will be displaced away from the stuffed atom towards the Ti atoms at the outer vertices of the orange tetrahedra in Fig. 7(d). Nevertheless, these changes still do not satisfy the normal oxygen bonding configurations with Ti^{4+} or Yb^{3+}. It therefore seems likely— and is indeed indicated by our EELS results—that replacement of Ti^{4+} by Yb^{3+} will result in one of the adjacent Ti atoms reducing to Ti^{3+} with an accompanying vacancy in that *1Ti3Yb* tetrahedron [highlighted red in Figs. 7(d) and 7(h)]. Still further changes in structure are possible such as static distortions of the cation framework, with the tetrahedron containing the oxygen vacancy expanding due to Coulomb repulsion. There are likely to be significant effects on the magnetic *4Yb* tetrahedra that surround the stuffed atom; there are six nearby *4Yb* tetrahedra, numbered in Fig. 7(d). We note that a study of

oxygen deficient $Y_2Ti_2O_7$ [10] found that *4Y* tetrahedra were much more likely to lose their oxygen atom, and it is thus possible that the oxygen vacancy in the red tetrahedron moves into the adjacent *4Yb* tetrahedron #2. In any case, tetrahedron #2 is most affected. It is clear from Figs. 7(e) and 7(g) that the replacement of a nonmagnetic Ti^{4+} cation by a magnetic Yb^{3+} can modify the nature of the magnetic exchange with the system through formation of the frustrated triangular lattice of magnetic cations. Furthermore, the introduction of a magnetic moment on the Ti site as a consequence of reduction of Ti^{4+} to magnetic Ti^{3+} as well as stuffing the Yb atom onto the Ti site will disrupt the magnetic order locally and may serve as pinning sites for magnetic defects (monopoles in spin-ice) within the material [10].

The differences between the three samples examined here can be interpreted in terms of such structural rearrangements. As shown in Fig. 8, the [2 1 1] atom columns can be also pictured as chains of tetrahedra. For both the Yb and Ti atom columns, the chain consists only of *2Ti2Yb* tetrahedra, whereas *M*1 is made of alternating pairs of *2Ti2Yb* and *4Yb* tetrahedra and *M*2 is made of alternating pairs of *2Ti2Yb* and *4Ti* tetrahedra. There are 10 cations in the repeat motif in all cases, and each atom column type has a different Yb : Ti ratio in its tetrahedral chain.

In a stuffed material, the oxygen atom inside a tetrahedron will be affected by all four atoms at its vertices, which means that the oxygen atoms close to any given [2 1 1] atom column depend upon the chains of tetrahedra shown in Fig. 8, not just the atoms in the column. The oxygen atoms are therefore very sensitive to stuffing. Furthermore, the difference in Yb : Ti ratio for each chain means that each has a different sensitivity.
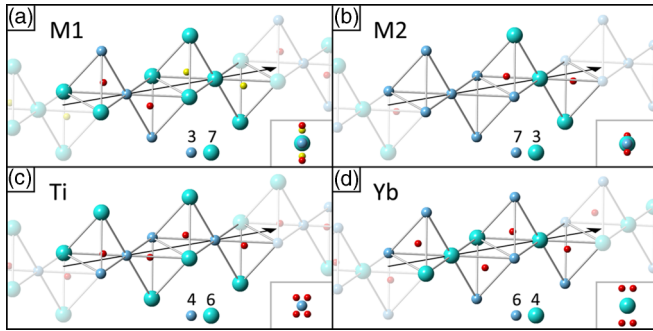
FIG. 8. The four types of [2 1 1] atom columns in $Yb_2Ti_2O_7$, shown as a chain of cation tetrahedra. The black arrow indicates the direction of propagation of the electron beam. Partial transparency highlights the repeat motif of 10 cations; the number of Ti (dark blue) and Yb (light blue) atoms in the motif is given at the bottom of each panel. The [2 1 1] projection of each column is inset bottom right. Color scheme is the same as Fig. 1.

Thus, using the same binomial statistics [Eq. (1)] for a 45 nm thick TEM specimen, and e.g. 1% stuffing and no antistuffing, we find that only 30% of M columns and 50% of Ti columns are directly affected by stuffing (obviously, no Yb columns are affected). However, the nearby oxygen atoms are affected in around 67% of M1 columns, 77% of Ti columns, 89% of Yb columns, and 92% of M2 columns. That is, the radial profiles of Yb and M2 columns should be more affected by stuffing than the Ti and M1 columns, and this does indeed appear to be the case in Figs. 4(g)–4(i). Furthermore, the structural rearrangements illustrated in Fig. 7 will tend to move oxygen atoms away from M1 columns more readily than M2 columns, producing the changes in radial profile shown in Figs. 4(g)–4(i).

Taken together, the modifications to the delicate balance of magnetic interactions, which result from the stuffing and changes in Ti valence that we have observed, will lead to a breakdown in the onset of long-range ferromagnetic order. These results are consistent with the magnetic properties of Sample 3 [Fig. 1(a)] showing no clear transition in the specific heat down to 50 mK.

V. CONCLUSIONS

We have examined three samples of $Yb_2Ti_2O_7$, with different low-temperature specific heat capacity anomalies that indicate varying magnetic properties, using aberration-corrected STEM. We find direct evidence for stuffing of Yb onto Ti sites, using atomic resolution EDX of Ti atomic columns that have anomalously bright contrast, in Sample 3. We also observe Yb atomic columns that have anomalously dark contrast, but are unable to use the well-known compositional sensitivity of ADF-STEM to extract the statistics of stuffing (or antistuffing) due to the confounding effects specimen thickness variations and/or surface damage. Nevertheless, we clearly observe the influence of oxygen atoms on these images, and by examining the radial intensity profile of cation columns, we observe rather different behavior of oxygen atoms near to the cation columns for the three samples. The sensitivity of the different types of atom column in the [2 1 1] ADF-STEM images is explained by considering them as chains of tetrahedra with different Ti : Yb ratios. The changes are consistent with the rearrangement of oxygen atoms away from Yb that occupies Ti sites. Using Ti-$L_{3,2}$ ELNES, we find that these differences in ADF-STEM radial intensity profile are accompanied by changes in Ti valence number, indicating the presence of magnetic Ti^{3+} and oxygen vacancies. Samples that have more diffuse specific heat capacity anomalies have more stuffing, lower Ti valence numbers, and more disordered oxygen sublattices.

The methods described here can readily be applied to other pyrochlore systems where a similar sensitivity to structural defects, including stuffing [9], has recently been shown to lead to significant differences in the magnetic behavior, for example, the magnetic ground state of the spin liquid candidate $Tb_2Ti_2O_7$ [61] and magnetic monopole dynamics in spin ice $Dy_2Ti_2O_7$ [62]. Studies of this kind should also prove useful in understanding the physics of other frustrated magnets where defects or low levels of doping rapidly modify the physics; examples include triangular lattice magnets, such as $CuFeO_2$ and $RbFe(MoO_4)_2$, and order-by-disorder transitions that occur in several lattice motifs.

More generally, such methods could play a valuable role in the study of emergent phenomena, including superconductivity and magnetism, both in the bulk and at interfaces, when defects are known to be important.

[1] J. S. Gardner, M. J. P. Gingras, and J. E. Greedan, Rev. Mod. Phys. **82**, 53 (2010).

[2] L. Pauling, J. Am. Chem. Soc. **57**, 2680 (1935).

[3] S. T. Bramwell and M. J. P. Gingras, Science **294**, 1495 (2001).

[4] J. E. Greedan, J. Alloys Compd. **408**, 444 (2006).

[5] J. N. Reimers, J. E. Greedan, and M. Sato, J. Solid State Chem. **72**, 390 (1988).

[6] H. D. Zhou, C. R. Wiebe, A. Harter, N. S. Dalal, and J. S. Gardner, J. Phys.: Condens. Matter **20**, 325201 (2008).

[7] H. Yamamura, H. Nishino, K. Kakinuma, and K. Nomura, Solid State Ionics **158**, 359 (2003).

[8] M. W. Gaultois, P. T. Barton, C. S. Birkel, L. M. Misch, E. E. Rodriguez, G. D. Stucky, and R. Seshadri, J. Phys.: Condens. Matter **25**, 186004 (2013).

[9] G. C. Lau, B. D. Muegge, T. M. McQueen, E. L. Duncan, and R. J. Cava, J. Solid State Chem. **179**, 3126 (2006).

[10] G. Sala, M. J. Gutmann, D. Prabhakaran, D. Pomaranski, C. Mitchelitis, J. B. Kycia, D. G. Porter, C. Castelnovo, and J. P. Goff, Nat. Mater. **13**, 488 (2014).

[11] K. A. Ross, T. Proffen, H. A. Dabkowska, J. A. Quilliam, L. R. Yaraskavitch, J. B. Kycia, and B. D. Gaulin, Phys. Rev. B **86**, 174424 (2012).

[12] K. A. Ross, L. Savary, B. D. Gaulin, and L. Balents, Phys. Rev. X **1**, 021002 (2011).

[13] A. Yaouanc, P. Dalmas de Réotier, C. Marin, and V. Glazkov, Phys. Rev. B **84**, 172408 (2011).

[14] H. W. J. Blöte, R. F. Wielinga, and W. J. Huiskamp, Physica **43**, 549 (1968).

[15] Y. Yasui, M. Soda, S. Iikubo, M. Ito, M. Sato, N. Hamaguchi, T. Matsushita, N. Wada, T. Takeuchi, N. Aso, and K. Kakurai, J. Phys. Soc. Jpn. **72**, 3014 (2003).

[16] L.-J. Chang, S. Onoda, Y. Su, Y.-J. Kao, K.-D. Tsuei, Y. Yasui, K. Kakurai, and M. R. Lees, Nat. Commun. **3**, 992 (2012).

[17] L.-J. Chang, M. R. Lees, I. Watanabe, A. D. Hillier, Y. Yasui, and S. Onoda, Phys. Rev. B **89**, 184416 (2014).

[18] E. Lhotel, S. R. Giblin, M. R. Lees, G. Balakrishnan, L. J. Chang, and Y. Yasui, Phys. Rev. B **89**, 224419 (2014).

[19] J. Gaudet, K. A. Ross, E. Kermarrec, N. P. Butch, G. Ehlers, H. A. Dabkowska, and B. D. Gaulin, Phys. Rev. B **93**, 064406 (2016).

[20] A. Yaouanc, P. D. de Reotier, L. Keller, B. Roessli, and A. Forget, J. Phys.: Condens. Matter **28**, 426002 (2016).

[21] M. J. P. Gingras and P. A. McClarty, Rep. Prog. Phys. **77**, 056501 (2014).

[22] R. Applegate, N. R. Hayre, R. R. P. Singh, T. Lin, A. G. R. Day, and M. J. P. Gingras, Phys. Rev. Lett. **109**, 097205 (2012).

[23] K. A. Ross, L. R. Yaraskavitch, M. Laver, J. S. Gardner, J. A. Quilliam, S. Meng, J. B. Kycia, D. K. Singh, Th. Proffen, H. A. Dabkowska, and B. D. Gaulin, Phys. Rev. B **84**, 174442 (2011).

[24] R. M. D'Ortenzio, H. A. Dabkowska, S. R. Dunsiger, B. D. Gaulin, M. J. P. Gingras, T. Goko, J. B. Kycia, L. Liu, T. Medina, T. J. Munsie, D. Pomaranski, K. A. Ross, Y. J. Uemura, T. J. Williams, and G. M. Luke, Phys. Rev. B **88**, 134428 (2013).

[25] J. A. Hodges, P. Bonville, A. Forget, A. Yaouanc, P. Dalmas de Réotier, G. André, M. Rams, K. Królas, C. Ritter, P. C. M. Gubbens, C. T. Kaiser, P. J. C. King, and C. Baines, Phys. Rev. Lett. **88**, 077204 (2002).

[26] J. S. Gardner, G. Ehlers, N. Rosov, R. W. Erwin, and C. Petrovic, Phys. Rev. B **70**, 180404 (2004).

[27] K. A. Ross, J. P. C. Ruff, C. P. Adams, J. S. Gardner, H. A. Dabkowska, Y. Qiu, J. R. D. Copley, and B. D. Gaulin, Phys. Rev. Lett. **103**, 227202 (2009).

[28] L. Savary and L. Balents, Phys. Rev. Lett. **108**, 037202 (2012).

[29] L. D. C. Jaubert, O. Benton, J. G. Rau, J. Oitmaa, R. R. P. Singh, N. Shannon, and M. J. P. Gingras, Phys. Rev. Lett. **115**, 267208 (2015).

[30] J. Robert, E. Lhotel, G. Remenyi, S. Sahling, I. Mirebeau, C. Decorse, B. Canals, and S. Petit, Phys. Rev. B **92**, 064425 (2015).

[31] K. Baroudi, B. D. Gaulin, S. H. Lapidus, J. Gaudet, and R. J. Cava, Phys. Rev. B **92**, 024110 (2015).

[32] M. A. Subramanian, G. Aravamudan, and G. V. S. Rao, Prog. Solid State Chem. **15**, 55 (1983).

[33] M. L. Hand, M. C. Stennett, and N. C. Hyatt, J. Eur. Ceram. Soc. **32**, 3211 (2012).

[34] See Supplemental Material at http://link.aps.org/supplemental/10.1103/PhysRevB.95.094431 for more STEM and EDX Results as well as Crystallographic Information.

[35] K. Kimoto, T. Asaka, T. Nagai, M. Saito, Y. Matsui, and K. Ishizuka, Nature **450**, 702 (2007).

[36] N. Li, K. Du, G. Liu, Y. Xie, G. Zhou, J. Zhu, F. Li, and H.-M. Cheng, J. Mater. Chem. A **1**, 1536 (2013).

[37] D. A. Muller, N. Nakagawa, A. Ohtomo, J. L. Grazul, and H. Y. Hwang, Nature **430**, 657 (2004).

[38] I. MacLaren and Q. M. Ramasse, Int. Mater. Rev. **59**, 115 (2014).

[39] P. Hartel, H. Rose, and C. Dinges, Ultramicroscopy **63**, 93 (1996).

[40] R. Ishikawa, A. R. Lupini, S. D. Findlay, and S. J. Pennycook, Microsc. Microanal. **20**, 99 (2014).

[41] Y.-M. Kim, J. He, M. D. Biegalski, H. Ambaye, V. Lauter, H. M. Christen, S. T. Pantelides, S. J. Pennycook, S. V. Kalinin, and A. Y. Borisevich, Nat. Mater. **11**, 888 (2012).

[42] K. Lu, E. Sourty, and J. Loos, J. Electron Microsc. **59**, 531 (2010).

[43] D. Wang, H. L. Xin, R. Hovden, H. Wang, Y. Yu, D. A. Muller, F. J. DiSalvo, and H. D. Abruna, Nat. Mater. **12**, 81 (2013).

[44] J. M. LeBeau, S. D. Findlay, L. J. Allen, and S. Stemmer, Nano Lett. **10**, 4405 (2010).

[45] S. Van Aert, J. Verbeeck, R. Erni, S. Bals, M. Luysberg, D. Van Dyck, and G. Van Tendeloo, Ultramicroscopy **109**, 1236 (2009).

[46] H. Kauko, C. L. Zheng, Y. Zhu, S. Glanvill, C. Dwyer, A. M. Munshi, B. O. Fimland, A. T. J. van Helvoort, and J. Etheridge, Appl. Phys. Lett. **103**, 232111 (2013).

[47] T. Mehrtens, K. Muller, M. Schowalter, D. Z. Hu, D. M. Schaadt, and A. Rosenauer, Ultramicroscopy **131**, 1 (2013).

[48] A. Rosenauer, T. Mehrtens, K. Müller, K. Gries, M. Schowalter, P. Venkata Satyam, S. Bley, C. Tessarek, D. Hommel, K. Sebald, M. Seyfried, J. Gutowski, A. Avramescu, K. Engl, and S. Lutgen, Ultramicroscopy **111**, 1316 (2011).

[49] M. Schowalter, I. Stoffers, F. F. Krause, T. Mehrtens, K. Mueller, M. Fandrich, T. Aschenbrenner, D. Hommel, and A. Rosenauer, Microsc. Microanal. **20**, 1463 (2014).

[50] V. Grillo, E. Carlino, and F. Glas, Phys. Rev. B **77**, 054103 (2008).

[51] R. F. Egerton, *Electron Energy Loss Spectroscopy in the Electron Microscope*, 3rd ed. (Springer, New York, 2011).

[52] J. Kirkland, *Advanced Computing in Electron Microscopy* (Springer, New York, 2010).

[53] P. W. Hawkes and J. C. H. Spence, *Science of Microscopy* (Springer-Verlag, New York, 2007), Vol. 1.

[54] J. M. LeBeau and S. Stemmer, Ultramicroscopy **108**, 1653 (2008).

[55] C. Koch, Ph.D., Arizona State University, 2002.

[56] A. Rosenauer and M. Schowalter, in *Microscopy of Semiconducting Materials 2007*, edited by A. G. Cullis and P. A. Midgley (Springer Netherlands, Dordrecht, 2008), p. 169.

[57] E. Eberg, A. T. J. van Helvoort, R. Takahashi, M. Gass, B. Mendis, A. Bleloch, R. Holmestad, and T. Tybell, J. Appl. Phys. **109**, 034104 (2011).

[58] E. Stoyanov, F. Langenhorst, and G. Steinle-Neumann, Am. Mineral. **92**, 577 (2007).

[59] J. M. Zhang, A. Visinoiu, F. Heyroth, F. Syrowatka, M. Alexe, D. Hesse, and H. S. Leipner, Phys. Rev. B **71**, 064108 (2005).

[60] L. A. Grunes, R. D. Leapman, C. N. Wilker, R. Hoffmann, and A. B. Kunz, Phys. Rev. B **25**, 7157 (1982).

[61] M. Ruminy, L. Bovo, E. Pomjakushina, M. K. Haas, U. Stuhr, A. Cervellino, R. J. Cava, M. Kenzelmann, and T. Fennell, Phys. Rev. B **93**, 144407 (2016).

[62] H. M. Revell, L. R. Yaraskavitch, J. D. Mason, K. A. Ross, H. M. L. Noad, H. A. Dabkowska, B. D. Gaulin, P. Henelius, and J. B. Kycia, Nat. Phys. **9**, 34 (2013).